Monthly Notices
of the
ROYAL ASTRONOMICAL SOCIETY

Mon. Not. R. Astron. Soc. **427,** 3044–3054 (2012) doi:10.1111/j.1365-2966.2012.21974.x

An optimal estimator for the CMB–LSS angular power spectrum and its application to *WMAP* and NVSS data

F. Schiavon,[1,2,3,4]★ F. Finelli,[3,4] A. Gruppuso,[3,4] A. Marcos-Caballero,[5,6] P. Vielva,[5] R. G. Crittenden,[7] R. B. Barreiro[5] and E. Martínez-González[5]

[1]*Dipartimento di Astronomia, Università degli Studi di Bologna, via Ranzani 1, I-40127 Bologna, Italy*
[2]*INAF-Istituto di Radioastronomia, via Gobetti 101, I-40129 Bologna, Italy*
[3]*INAF-IASF Bologna, Istituto di Astrofisica Spaziale e Fisica Cosmica di Bologna via Gobetti 101, I-40129 Bologna, Italy*
[4] *INFN, Sezione di Bologna, Via Berti Pichat 6/2, I-40127 Bologna, Italy*
[5]*Instituto de Física (CSIC – Universidad de Cantabria), Avda. Los Castros s/n, E-39005 Santander, Spain*
[6]*Departamento de Física Moderna, Facultad de Ciencias, Universidad de Cantabria, Avda. Los Castros s/n, E-39005 Santander, Spain*
[7]*Institute of Cosmology and Gravitation, University of Portsmouth, Dennis Sciama Building, Burnaby Rd, Portsmouth, Hampshire PO1 3FX*

Accepted 2012 August 22. Received 2012 August 12; in original form 2012 June 11

ABSTRACT

We use a quadratic maximum likelihood (QML) method to estimate the angular power spectrum of the cross-correlation between cosmic microwave background and large-scale structure maps as well as their individual auto-spectra. We describe our implementation of this method and demonstrate its accuracy on simulated maps. We apply this optimal estimator to *Wilkinson Microwave Anisotropy Probe* (*WMAP*) 7-yr and National Radio Astronomical Observatory (NRAO) Very Large Array Sky Survey (NVSS) data and explore the robustness of the angular power spectrum estimates obtained by the QML method. With the correction of the declination systematics in NVSS, we can safely use most of the information contained in this survey. We then make use of the angular power spectrum estimates obtained by the QML method to derive constraints on the dark energy critical density in a flat Λ cold dark matter model by different likelihood prescriptions. When using just the cross-correlation between *WMAP* 7-yr and NVSS maps with $1^\circ.8$ resolution, the best-fitting model has a cosmological constant of approximately 70 per cent of the total energy density, disfavouring an Einstein–de sitter universe at more than 2σ confidence level.

Key words: methods: numerical – methods: statistical – cosmic background radiation – cosmology: observations – large-scale structure of Universe.

1 INTRODUCTION

Understanding of the nature of dark energy is one of the outstanding questions in observational cosmology. Since the discovery of the present acceleration of the Universe by the measurement of the luminosity distance of distant Type Ia supernovae (SN Ia; Riess et al. 1998; Perlmutter et al. 1999), several observations (e.g. Tegmark et al. 2004; Eisenstein et al. 2005; Larson et al. 2011) have converged to a cosmological concordance model in which an unknown component having a negative pressure density – 'dark energy' – that contributes ∼2/3 of the total energy budget of the Universe. At present the precise nature of dark energy, parametrized by its equation of state, can only be weakly constrained using a range of cosmological tests, but indications are that its behaviour is close to that expected from a cosmological constant.

A key strategy in determining the nature of dark energy is to combine as many different observations as possible, including the luminosity distances for SN Ia, the baryonic acoustic oscillation (BAO) scale observed in galaxy surveys, anisotropies of the cosmic microwave background (CMB) and weak lensing surveys. Cross-correlations among the above observations also contain precious cosmological information about dark energy. Ambitious space projects have been proposed to address the dark energy question with this strategy, including *Euclid* (Laureijs et al. 2009), which will focus on BAO and weak lensing, and *WFIRST*,[1] an infrared satellite with a focus yet to be specified. In the meantime, ground-based programmes such as DES,[2] PanSTARRS,[3] LSST[4] and JAPS[5] will also improve the current understanding of structure formation and provide excellent galaxy surveys to cross-correlate with the CMB anisotropy maps from Planck (Planck Collaboration 2006).

★E-mail: f.schiavon@ira.inaf.it

[1] http://wfirst.gsfc.nasa.gov
[2] http://www.darkenergysurvey.org/
[3] http://pan-starrs.ifa.hawaii.edu/public/
[4] http://www.lsst.org/lsst/
[5] http://jpas.astro.ufsc.br/

One of the key indicators of the presence of dark energy is CMB fluctuations created by the late integrated Sachs–Wolfe (ISW) effect (Sachs & Wolfe 1967). When the Universe undergoes the transition period between the matter dominated and the dark energy dominated era,[6] secondary CMB anisotropies are created at late times and these contribute most at large angular scales (Kofman & Starobinsky 1985). Since the low multipoles of the CMB angular power spectrum (APS) are mostly affected by cosmic variance, an extraction of the ISW part solely from CMB data is rather difficult, but it is feasible when CMB is cross-correlated with large-scale structure (LSS) (Crittenden & Turok 1995). Several positive detections of the ISW–LSS cross-correlation have been performed since the release of the *WMAP* first year data by using different tracers of LSS and statistical estimators (e.g. Boughn et al. 2002; Fosalba, Gaztañaga & Castander 2003; Afshordi, Loh & Strauss 2004; Boughn & Crittenden 2004; Nolta at al. 2004; Pietrobon, Balbi & Marinucci 2006; Vielva, Martínez-González & Tucci 2006; McEwen et al. 2007, 2008; Giannantonio et al. 2008; Ho et al. 2008; Francis & Peacock 2010; Hernandez-Monteagudo 2010; Dupé et al. 2011, and references therein).

One of the purposes of this paper is to develop tools to estimate the APS of the cross-correlation between CMB and LSS by a quadratic maximum likelihood (QML) method. The QML method in this context has a number of advantages: foremost, given the low signal-to-noise ratio expected for the ISW–LSS cross-correlation, it is essential to use a minimum variance method, such as QML, to estimate the cross-correlation power spectrum. In addition, being based in pixel space, the QML method is ideal for accounting for the incomplete sky coverage and masks of the surveys. Finally, while the QML method is expensive computationally, the fact that the ISW signal is primarily at low multipoles means that it is tractable to constrain it on maps using only a modest resolution. The QML method has also found application in the estimation of the power spectrum of the CMB intensity and polarization (Tegmark 1997; Tegmark & de Oliveira-Costa 2001) and has been recently applied to the latest releases of *WMAP* data (Gruppuso et al. 2009, 2011; Paci et al. 2010). A QML estimator was already used to measure the CMB–LSS cross-correlation only by Padmanabhan et al. (2005); however, our implementation is different in few important aspects: the inversion of the matrices is implemented here using the single value decomposition (see also Section 3.1) and all the three spectra – TT, TG, GG – are computed for all the multipoles in the range of interest.

Another purpose of this work is to apply our methodology to available public CMB and LSS data, namely *WMAP* 7-yr (Jarosik et al. 2011) and National Radio Astronomical Observatory (NRAO) Very Large Array (VLA) Sky Survey (NVSS) data (Condon et al. 1998). NVSS has been one of the most widely used surveys in the context of ISW studies because the radio galaxies it surveys are at high redshifts and it covers a large sky fraction of the sky; however, contradicting claims about the evidence of its non-vanishing correlation with CMB exist in the literature (Pietrobon et al. 2006; Hernandez-Monteagudo 2010; Sawangwit et al. 2010, see also Dupé et al. 2011 for an exhaustive compilation of existing results). It is therefore important to apply an optimal methodology to address and quantify the evidence of cross-correlation between the most recent large-scale CMB measurement and one of the largest LSS surveys available.

[6] Similarly, there is an *early* ISW effect connected to the radiation to matter transition and the free streaming of neutrinos.

Our paper is organized as follows. In Section 2 we describe the QML method and give technical details of our implementation of it and Section 3 discusses our tests of the implementation in simulated maps. In Section 4 we report the APS estimates obtained from *WMAP* 7-yr and NVSS data, and then we use these estimates of the cross-correlation in Section 5 to derive constraints on the present critical density due to the cosmological constant. Finally, in Section 6 we draw our conclusions.

2 METHODOLOGY

2.1 The QML approach

The QML method for the power spectrum estimate of CMB anisotropies was introduced by Tegmark (1997) and later extended to polarization by Tegmark & de Oliveira-Costa (2001). Previously, a QML method was employed to measure the cross-correlation between CMB and LSS by Padmanabhan et al. (2005, see also Ho et al. 2008). The code in Padmanabhan et al. (2005) estimated the cross-correlation power spectrum only, with a fast and approximated algorithm to invert matrices and used the approximation of a block diagonal covariance matrix. In what follows we shall describe the QML method for the whole CMB–LSS data and our implementation which does not depend on the simplifying assumptions used in Padmanabhan et al. (2005).

Given a CMB map in temperature and a galaxy survey $\boldsymbol{x} = (\mathrm{T}, \mathrm{G})$ (vector in pixel space), the QML provides an estimator of the APS $\hat{C}_\ell^X$ – with X being one of TT, TG, GG. This estimator is given by

$$\hat{C}_\ell^X = \sum_{\ell' X'} \left(\mathbf{F}^{-1}\right)_{\ell\ell'}^{XX'} \left[\boldsymbol{x}^t \mathbf{E}_{\ell'}^{X'} \boldsymbol{x} - \mathrm{tr}\left(\mathbf{N}\mathbf{E}_{\ell'}^{X'}\right)\right], \tag{1}$$

where $\mathbf{F}_{\ell\ell'}^{XX'}$ is the Fisher matrix defined as

$$\mathbf{F}_{\ell\ell'}^{XX'} = \frac{1}{2}\mathrm{tr}\left[\mathbf{C}^{-1}\frac{\partial \mathbf{C}}{\partial C_\ell^X}\mathbf{C}^{-1}\frac{\partial \mathbf{C}}{\partial C_{\ell'}^{X'}}\right], \tag{2}$$

and the $\mathbf{E}$ matrix is given by

$$\mathbf{E}_\ell^X = \frac{1}{2}\mathbf{C}^{-1}\frac{\partial \mathbf{C}}{\partial C_\ell^X}\mathbf{C}^{-1}, \tag{3}$$

$\mathbf{C} = \mathbf{S}(C_\ell^X) + \mathbf{N}$ being the total global covariance matrix including the signal $\mathbf{S}$ and noise $\mathbf{N}$ contributions. C_ℓ^X is called the fiducial theoretical power spectrum and is also used to create the simulated maps used to test the method in Section 3.

Although an initial assumption is needed for this fiducial power spectrum, the QML method provides unbiased estimates of the power spectrum of the map regardless of this initial guess

$$\left\langle \hat{C}_\ell^X \right\rangle = C_\ell^{X,\mathrm{obs}}. \tag{4}$$

Here, the average is taken over the ensemble of realizations based on the input power spectrum of the map $C_\ell^{X,\mathrm{obs}}$. (See Section 3 for more details.) The assumed fiducial power spectrum can impact the error estimates, but in practice we start near enough to the true result to be able to neglect this effect. The QML method is also optimal, since it can provide the smallest error bars allowed by the Fisher–Cramer–Rao inequality,

$$\left\langle \Delta\hat{C}_\ell^X \Delta\hat{C}_{\ell'}^{X'} \right\rangle = \left(\mathbf{F}^{-1}\right)_{\ell\ell'}^{XX'}, \tag{5}$$

where

$$\Delta\hat{C}_{\ell'}^{X'} = \hat{C}_\ell^X - \left\langle \hat{C}_\ell^X \right\rangle, \tag{6}$$

and the averages, as above, are over an ensemble of realizations.

Our implementation of the QML method (named BOLISW) is fully parallelized (MPI) and written in FORTRAN 90. The inversion of the covariance matrix $\mathbf{C}$ scales as $\mathcal{O}(N_{\rm pix}^3)$. The number of operations is roughly driven, once the inversion of the total covariance matrix is done, by the matrix–matrix multiplications to build the operators $\mathbf{E}_\ell^X$ in equation (3) and by calculating the Fisher matrix $\mathbf{F}_{\ell\ell'}^{XX'}$ given in equation (2). The number of operations that are needed to build these matrices scales as $\mathcal{O}(\mathcal{N}_{\rm pix}^{\gamma\in})$. This scaling makes clear that the QML method can treat only a limited number of pixels. Therefore, in the context of all-sky observations it can be applied only at modest resolution.

2.2 Fiducial spectra

For our fiducial model, we assume the concordance Λ cold dark matter (ΛCDM) model, with parameters derived from the *WMAP*7 best fit. Throughout this work, we assume an equation of state of the dark energy fixed at $w = -1$. With these assumptions, it is straightforward to calculate the expected power spectra $C_\ell^{\rm GG}$ and $C_\ell^{\rm TG}$:

$$C_\ell^{\rm GG} = 4\pi \int \frac{{\rm d}k}{k} \Delta^2(k) I_\ell^{\rm G^2}(k), \tag{7}$$

$$C_\ell^{\rm TG} = 4\pi \int \frac{{\rm d}k}{k} \Delta^2(k) I_\ell^{\rm ISW}(k) I_\ell^{\rm G}(k), \tag{8}$$

respectively. $\Delta^2(k)$ is the logarithmic matter primordial power spectrum, and the filters of the galaxy density distribution ($I_\ell^{\rm G}$) and the ISW ($I_\ell^{\rm ISW}$) are given by

$$I_\ell^{\rm G}(k) = \int {\rm d}z\, b(z) \frac{{\rm d}N}{{\rm d}z} \delta_M(k, z) j_\ell\left(k\chi(z)\right), \tag{9}$$

$$I_\ell^{\rm ISW}(k) = -2 \int {\rm d}z\, {\rm e}^{-\tau} \frac{{\rm d}\Phi}{{\rm d}z} j_\ell\left(k\chi(z)\right). \tag{10}$$

Here, $\frac{{\rm d}N}{{\rm d}z}$ is the redshift distribution of the galaxy survey in question, and we have implicitly used the fact that the density contrast in the galaxy survey tracks the matter density contrast as

$$\delta_{\rm G}(\hat{n}) = \int {\rm d}z\, b(z) \frac{{\rm d}N}{{\rm d}z} \delta_M(\hat{\boldsymbol{n}}, z). \tag{11}$$

It is well known that the late ISW–LSS cross-correlation depends not only on the matter fluctuations on large scales, but also on how these are related to the observed galaxy distribution determined by the product $b(z){\rm d}N/{\rm d}z$. This can be simultaneously estimated using the measurement of $C_\ell^{\rm GG}$, also exploiting the QML method.

2.3 Numerical improvements

For the reasons discussed above, the QML method is quite computationally expensive and prohibitive at high resolution. We discuss here some changes which can improve the numerics and decrease substantially the execution time with a negligible loss of accuracy.

The predicted $C_\ell^{\rm TG}$ is generally non-zero, and its measurement is the primary object of the ISW measurements. However, it is expected to be relatively small, even for the largest scales, so it is a good approximation to assume $C_\ell^{\rm TG} = 0$ for the fiducial model, which is used to build the covariance matrix. Further, the noise matrix $\mathbf{N}$ may be assumed to be uncorrelated between the CMB and the galaxy measurements. Under these assumptions, the Fisher matrix becomes block diagonal and the three spectra $\hat{C}_\ell^{\rm TT}$, $\hat{C}_\ell^{\rm TG}$ and $\hat{C}_\ell^{\rm GG}$ can be estimated independently from each other. This reduces the computation cost of the Fisher matrix by 50 per cent with respect to the problem with the full covariance. Moreover, estimating just $\hat{C}_\ell^{\rm TG}$ the computational cost of the problem decreases by a further factor of 1/6, as in Padmanabhan et al. (2005).

In order to apply the algebra of the QML method, described in equations (1)–(3), one must build the covariance matrix $\mathbf{C}$ in pixel space and the Fisher matrix $\mathbf{F}$ in ℓ space. The latter is the most expensive task computationally, largely because it requires the inversion of the pixel space covariance matrix $\mathbf{C}$. This inversion can also introduce numerical errors since its eigenvalues naively span several orders of magnitude.

To bypass this issue, we have used inversion routines only on numerically homogeneous blocks thanks to the following expressions. Given a general matrix $\mathbf{A}$ in block form

$$\mathbf{A} = \begin{pmatrix} \mathbf{A}_{11} & \mathbf{A}_{12} \\ \mathbf{A}_{21} & \mathbf{A}_{22} \end{pmatrix}, \tag{12}$$

where $\mathbf{A}_{11}$ and $\mathbf{A}_{22}$ are non-singular square matrices, then it can be shown that the inverse of $\mathbf{A}$ is

$$\mathbf{A}^{-1} = \begin{pmatrix} \mathbf{B}_{11} & -\mathbf{B}_{11}\mathbf{A}_{12}\mathbf{A}_{22}^{-1} \\ -\mathbf{A}_{22}^{-1}\mathbf{A}_{21}\mathbf{B}_{11} & \mathbf{A}_{22}^{-1} + \mathbf{A}_{22}^{-1}\mathbf{A}_{21}\mathbf{B}_{11}\mathbf{A}_{12}\mathbf{A}_{22}^{-1} \end{pmatrix}, \tag{13}$$

with

$$\mathbf{B}_{11} = \left(\mathbf{A}_{11} - \mathbf{A}_{12}\mathbf{A}_{22}^{-1}\mathbf{A}_{21}\right)^{-1}. \tag{14}$$

For our purposes, we partition the TT, TG and GG blocks of $\mathbf{C}$, so that $\mathbf{A}_{11}$ is the covariance related to the CMB temperature sector and $\mathbf{A}_{22}$ relates to the covariance of the galaxy sector. Thus, assuming a fiducial model without any cross-covariance simplifies the inversion calculation significantly. This technique is also applied to the Fisher matrix inversion in multipole space (with $\mathbf{A}_{11} = \mathbf{F}_{\ell\ell'}^{\rm TT}$), obtaining a much better precision with respect to the brute force inversion.

3 VALIDATION WITH SIMULATED MAPS

In order to test our implementation of the QML method, we created simulated galaxy count maps and CMB temperature anisotropies following the recipe described in Boughn, Crittenden & Turok (1998, see also Barreiro et al. 2008; Giannantonio et al. 2008). We employ the HEALPIX[7] program SYNFAST (Gorski et al. 2005) which allows one to create $a_{\ell m}$ such that

$$\left\langle a_{\ell m}^Y a_{\ell' m'}^{Y'\,\star} \right\rangle = C_\ell^{YY'} \delta_{\ell\ell'} \delta_{mm'}, \tag{15}$$

where $Y, Y' = {\rm T}, {\rm G}$. The total map for the CMB anisotropies $a_{\ell m}^{\rm T}$ is simulated as the sum of three different maps

$$a_{\ell m}^{\rm T} = a_{\ell m}^{\rm ISWc} + a_{\ell m}^{\rm ISWu} + a_{\ell m}^{\rm prim}, \tag{16}$$

where $a_{\ell m}^{\rm ISWc}$ represents the fully correlated ISW effect with the galaxy distribution, $a_{\ell m}^{\rm ISWu}$ is the uncorrelated part of the ISW effect and $a_{\ell m}^{\rm prim}$ is the primordial CMB signal. These amplitudes are given by

$$a_{\ell m}^{\rm ISWc} = \xi_a \frac{C_\ell^{\rm TG}}{\sqrt{C_\ell^{\rm GG}}}, \tag{17}$$

$$a_{\ell m}^{\rm ISWu} = \xi_b \sqrt{C_\ell^{\rm ISW} - \frac{(C_\ell^{\rm TG})^2}{C_\ell^{\rm GG}}}, \tag{18}$$

[7] http://healpix.jpl.nasa.gov/

$$a_{\ell m}^{\rm prim} = \xi_c \sqrt{C_\ell^{\rm TT} - C_\ell^{\rm ISW}}. \quad (19)$$

In addition, for the galaxy count maps we consider

$$a_{\ell m}^{\rm G} = \xi_a \sqrt{C_\ell^{\rm GG}}, \quad (20)$$

where ξs are Gaussianly distributed complex random numbers, with zero mean and unit variance. They are the seeds of the simulations and satisfy $\langle \xi_a \xi_{a'}^* \rangle = \delta_{aa'}$. In this way it can be shown that

$$\langle a_{\ell m}^{\rm T} a_{\ell m}^{\rm T*} \rangle = C_\ell^{\rm TT}, \quad (21)$$

$$\langle a_{\ell m}^{\rm G} a_{\ell m}^{\rm G*} \rangle = C_\ell^{\rm GG}. \quad (22)$$

$$\langle a_{\ell m}^{\rm T} a_{\ell m}^{\rm G*} \rangle = C_\ell^{\rm TG}. \quad (23)$$

We have tested the QML approach using these Monte Carlo simulations. In particular, we have performed 3000 realizations for CMB and LSS correlated maps at the HEALPIX resolution of $N_{\rm side} = 32$.[8] For the multipoles, we consider the range $\Delta\ell = [2, 95]$, i.e. up to the Nyquist frequency $3N_{\rm side} - 1$. The standard ΛCDM cosmological model (Larson et al. 2011) is assumed, as well as a survey with characteristics similar to the NVSS catalogue (Condon et al. 1998), namely a similar sky coverage (see the next section), a galaxy density number distribution per redshift given by the Ho et al. (2008) model and a bias $b = 1.98$.

These simulated maps show that our QML implementation leads to unbiased and minimum variance results when considering the realistic case of a masked sky, as can be seen by comparing the simulations to the projected errors from the Fisher matrix. Importantly, we confirm that the method is unbiased and has minimum variance when the signal covariance matrix is block diagonal, i.e. when fiducial cross-correlation power spectrum $C_\ell^{\rm TG}$ is set to zero: with the latter approximation, no difference can be appreciated by eye on the QML estimates and a very small difference can be seen in the likelihood constructed from the Fisher matrix, which will be shown for our application to real maps of *WMAP* 7 yr and NVSS in Section 5.

It is important to note that, while on these large scales the noise contribution in *WMAP* and future (Planck) CMB temperature maps is so low that the CMB noise $\mathbf{N}$ can be safely neglected, this is not necessarily true for LSS surveys. Depending on the number of sources used as large-scale tracers, the galaxy density map could be significantly affected by Poissonian noise, which must be taken into account.

The results from the Monte Carlo validation are summarized in Fig. 1: the upper, middle and lower panels show, respectively, the average estimates for the TT, GG and TG spectra derived from the Monte Carlo simulations. Three different scenarios are considered, all of which provide unbiased averaged estimates in good agreement with the fiducial model (blue lines) and they differ only in their error bars. The first case corresponds to a masked sky (accounting for the NVSS sky coverage and the *WMAP* KQ75 mask – we use two different masks, each mask is used with the proper map) with negligible Poissonian shot-noise contribution to the LSS map (given by the thick error bars), secondly, a full-sky case with a shot noise like that expected in NVSS (see the next section for more details) when only sources above 2.5 mJy are taken into account (solid line error bars) and, finally a more realistic situation where both the incomplete sky and the shot noise are included in the analysis (light dark error bars). The error bars increase when the noise level in the LSS map rises and when the fraction of the sky considered is reduced, the latter falling approximately with $\sqrt{f_{\rm sky}^{\rm T} f_{\rm sky}^{\rm G}}$, as expected.

For comparison, the plots also include the average ANAFAST estimation for the full-sky case (dark lines), based on the simple HEALPIX FFT tool. As can be seen, the ANAFAST estimation is slightly biased at high ℓ in the two auto-spectra.

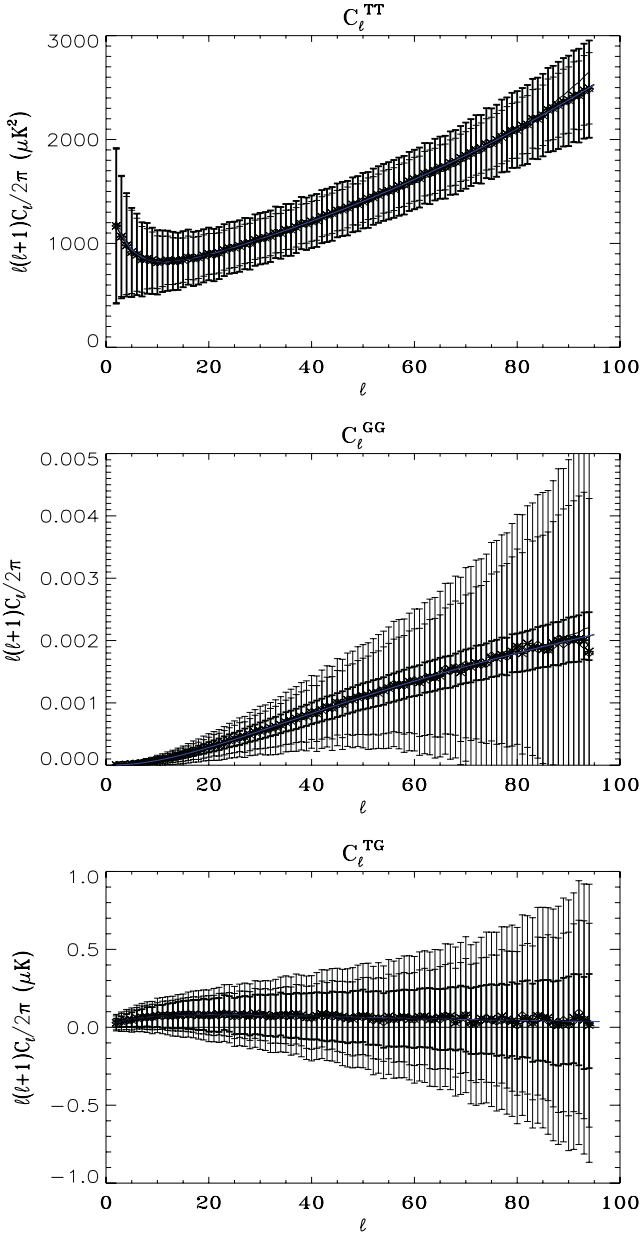

Figure 1. The average estimates for the Monte Carlo validation: the upper and middle panels show the TT and GG auto-spectra, respectively, and the lower one is the TG cross-spectrum. We compare results for three cases: using realistically masked maps without noise in the LSS maps (thick error bars), using full-sky maps with NVSS-like shot noise (solid line error bars), and assuming both masked maps and NVSS-like shot noise (light dark error bars). We can see that average power spectra from the QML all agree very well with the underlying fiducial theoretical power spectra (blue lines). The error bars change according to the noise level in the LSS map and the fraction of the sky considered. The dark lines are the average of the ANAFAST estimates, which are slightly biased at high ℓ in the two auto-spectra.

[8] The number of pixels $N_{\rm pix}$ is related to the parameter $N_{\rm side}$ through $N_{\rm pix} = 12N_{\rm side}^2$.

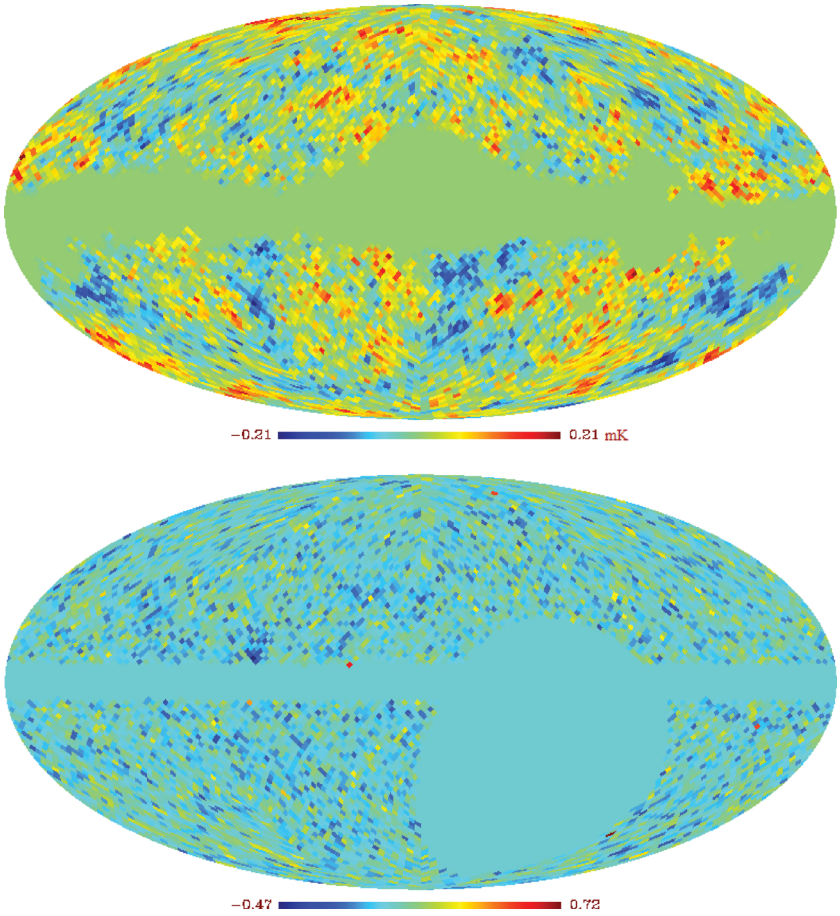

Figure 2. *WMAP* 7-yr (top) and NVSS (bottom) maps at HEALPIX resolution $N_{\rm side} = 32$ used in this analysis, with the respective masks. In the displayed NVSS map, the threshold flux is 2.5 mJy and the corrections for systematics in declination have been applied.

4 APPLICATION TO *WMAP* 7-YR AND NRAO VLA SKY SURVEY DATA

In this section, we describe the application of our QML code to estimating the cross-correlation spectrum between the *WMAP* 7-yr CMB maps and the NVSS data.

4.1 The maps

For *WMAP* data we make use of publicly available products.[9] In particular, clean maps at the *V* and *W* frequency bands have been co-added, using a weighting procedure that accounts for the instrumental noise variance per pixel (see Fig. 2, top panel). These frequency maps have been cleaned following a template fitting approach (Gold et al. 2011), and are those used by the *WMAP* team to perform cosmological tests, such as constraining non-Gaussianity (Komatsu et al. 2011). The co-added map has been degraded from its original $N_{\rm side} = 1024$ down to $N_{\rm side} = 32$, since the angular scales associated with this resolution ($\approx 2^\circ$) are enough to capture almost all the signals in the CMB–LSS cross-correlation expected from the ISW effect. Following this, the *WMAP* KQ75 Galactic mask (similarly degraded) is applied to the co-added map, in order to mitigate the unavoidable foreground contamination in regions within and near the Galactic plane, and also to remove known and intense extragalactic objects such as the Magellanic clouds and large clusters near the Northern Galactic Pole. Finally, the remaining monopole and dipole moments outside the mask have been estimated and removed.

The NVSS catalogue (Condon et al. 1998) is a radio sample at 1.4 GHz produced with the VLA (see Fig. 2, bottom panel). It covers ≈85 per cent of the sky, up to an equatorial declination of $\delta > -40^\circ$. The original survey accounts for $\approx 2 \times 10^6$ sources with fluxes >2.5 mJy. This survey has been widely used in the context of the ISW studies. It was first used by Boughn & Crittenden (2002) to probe the CMB–LSS cross-correlation with the *COBE* data, and a few years afterwards it was successfully used by the same authors with *WMAP* data, in the first work reporting such cross-correlation (Boughn & Crittenden 2004); this was soon followed by Nolta et al. (2004) with a similar analysis by the *WMAP* team.

The survey has a somewhat inhomogeneous sensitivity as a function of the equatorial declination (see Condon et al. 1998 for details), resulting in the mean galaxy density that artificially varies with the declination. Therefore, some pre-processing is needed in order to mitigate this large-scale effect. One of the procedures used in the literature consists of defining iso-latitude bands (in equatorial coordinates) and imposing that these bands have the same mean galaxy density. In our case, this pre-processing consists of selecting first the sources above a particular flux cut and then defining nine bands of equal area, imposing the same mean galaxy density number for

[9] http://lambda.gsfc.nasa.gov/

each band. Finally, we rotate to Galactic coordinates to compare to *WMAP*, and then pixelize to a HEALPIX resolution of $N_{\rm side} = 32$.

Previous works (e.g. Nolta et al. 2004; Vielva et al. 2006) have shown that the particularities of this pre-processing do not affect significantly the results and we confirm this below. We also repeat the analysis for different thresholds in flux, namely 2.5, 5, 10 mJy, as the higher flux thresholds should be less sensitive to possible declination systematics.

4.2 Source redshift distribution

To interpret the results of our measurements, we must assume some redshift distribution $\mathrm{d}N/\mathrm{d}z$ and potentially redshift-dependent bias $b(z)$ for the sample. Given a redshift distribution, the average bias can be estimated from the measured QML estimates for $C_\ell^{\rm GG}$; however, here we exploit previous measurements for the NVSS sample.

Historically, the redshift distribution was based on models of the sources by Dunlop & Peacock (1990), and a time-independent bias of 1.6 was derived by Boughn & Crittenden (2002). A larger time-independent bias was found by Blake, Ferreira & Borrill (2004), albeit with a different redshift distribution than used by Boughn & Crittenden (2002). In Ho et al. (2008), a new redshift distribution was derived based on a Γ distribution fit which was constrained to give the cross-correlations measured between the NVSS survey and Sloan Digital Sky Survey (SDSS) Luminous Red Galaxy (LRG) subsamples:

$$\frac{\mathrm{d}N^{\rm Ho}}{\mathrm{d}z} = \frac{\alpha^\alpha}{z_*^{\alpha+1}\Gamma(\alpha)} z^\alpha \mathrm{e}^{-\alpha z/z_*}, \tag{24}$$

where $z_* = 0.79$ and $\alpha = 1.18$.[10] Ho et al. (2008) also estimate an effective, redshift-independent value for the bias as $b(z) = 1.98$. Finally, we also explore the most recent galaxy redshift distribution proposed by de Zotti et al. (2010): a fourth-order polynomial fit to the Combined EIS–NVSS Survey of Radio Sources (CENSORS) distribution (Brookes et al. 2008):

$$\frac{\mathrm{d}N^{\mathrm{d}Z}}{\mathrm{d}z} = 1.29 + 32.37z - 32.89z^2 + 11.13z^3 - 1.25z^4\,. \tag{25}$$

A comparison of the two redshift distributions based on equations (24) and (25) is shown in Fig. 3. For the redshift distribution in equation (25) we consider a redshift-dependent bias (Matarrese et al. 1997; Moscardini et al. 1998):

$$b(z) = b_0 + \frac{b_1}{D^\gamma(z)} \tag{26}$$

where $D(z)$ is the linear growth factor in a ΛCDM universe. Following Xia et al. (2010a), we choose $b_0 = 1.1$, $b_1 = 0.6$, $\gamma = 1$. Below we focus on the latter two distributions, and examine how the uncertainties impact the derived cosmological constraints.

4.3 Measurements of the spectra

In Fig. 4 we present the TT, GG and TG spectra obtained by our QML method up to $\ell = 64$ ($=2N_{\rm side}$) for the 2.5 mJy flux cut in NVSS data. Since the signal-to-noise ratio for the unbinned TG power spectrum is rather poor, we present also the binned power spectrum $C_{\rm b}^{\rm TG}$ over $\Delta\ell = 9$. The binned estimates are simply the average of the unbinned estimates inside the bin. For plotting purposes, we associate $\sqrt{\sum_{\ell\in\Delta\ell}(\mathbf{F}^{-1})_{\ell\ell}^{\rm TG\,TG}/[N(N-1)]}$ for the uncertainty in the binned estimate. Unless otherwise stated, all the maps have been corrected for the declination effect.

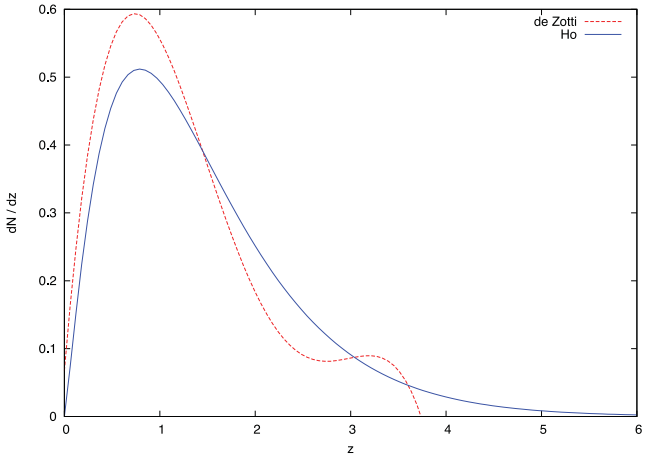

Figure 3. Comparison of the source redshift distribution used in Ho et al. (2008) (blue solid line) and the one with a redshift-dependent bias with assuming the CENSORS source distribution (red dotted line).

To investigate potential systematic problems, we compare the dependence of the TG and GG spectra on the different threshold fluxes for NVSS considered here in Fig. 5 (TT is not shown since it is of course unchanged). Overall the APS estimates – already corrected by removing the Poissonian noise – agree very well when varying the flux threshold, with larger error bars for larger flux threshold, as expected given the fewer objects and resulting larger Poisson errors. In Fig. 6 we examine the importance of the correction for declination systematics in NVSS for a flux cut of 10 mJy. Our result for GG agrees with Blake & Wall (2002), confirming that with a conservative flux cut of 10 mJy the declination systematics in NVSS is negligible.

Finally, in Fig. 7 we compare the GG and TG results obtained by assuming the two redshift distributions in equations (24) and (25), including also the dependence of the bias on the redshift in the latter case. The QML estimates are stable with respect to such different physical assumptions in the two fiducial power spectra. By considering the more physical scenario in which the bias evolves in redshift, the tension between the NVSS auto-spectrum and the theoretical predictions could be partially alleviated.

We note few important findings in our estimates of the APS of the *WMAP* 7 yr–NVSS cross-correlation. First, the estimate of the GG power spectrum in the NVSS map is larger than our fiducial model. Moreover, we note a deficit in the QML TT estimates at low multipoles, which is consistent with the *WMAP* TT estimates publicly available.

Our estimates for the NVSS auto-power spectrum are larger, but consistent within the errors, than those obtained by Blake et al. (2004), who used a similar optimal estimator on a map of the same resolution. The stability of the $C_\ell^{\rm GG}$ estimates with respect to different flux threshold is fully consistent with what found in Blake et al. (2004).

As yet it is unclear whether this deviation could be caused by some systematics in the NVSS data or should be ascribed to a genuine physical effect, as an effective bias larger than $\sim$2, which is usually assumed. Xia et al. (2010a) estimated a larger discrepancy at lower multipoles and explained this effect as a result of

[10] Note that we have corrected the normalization factor of the Γ distribution assumed in Ho et al. (2008).

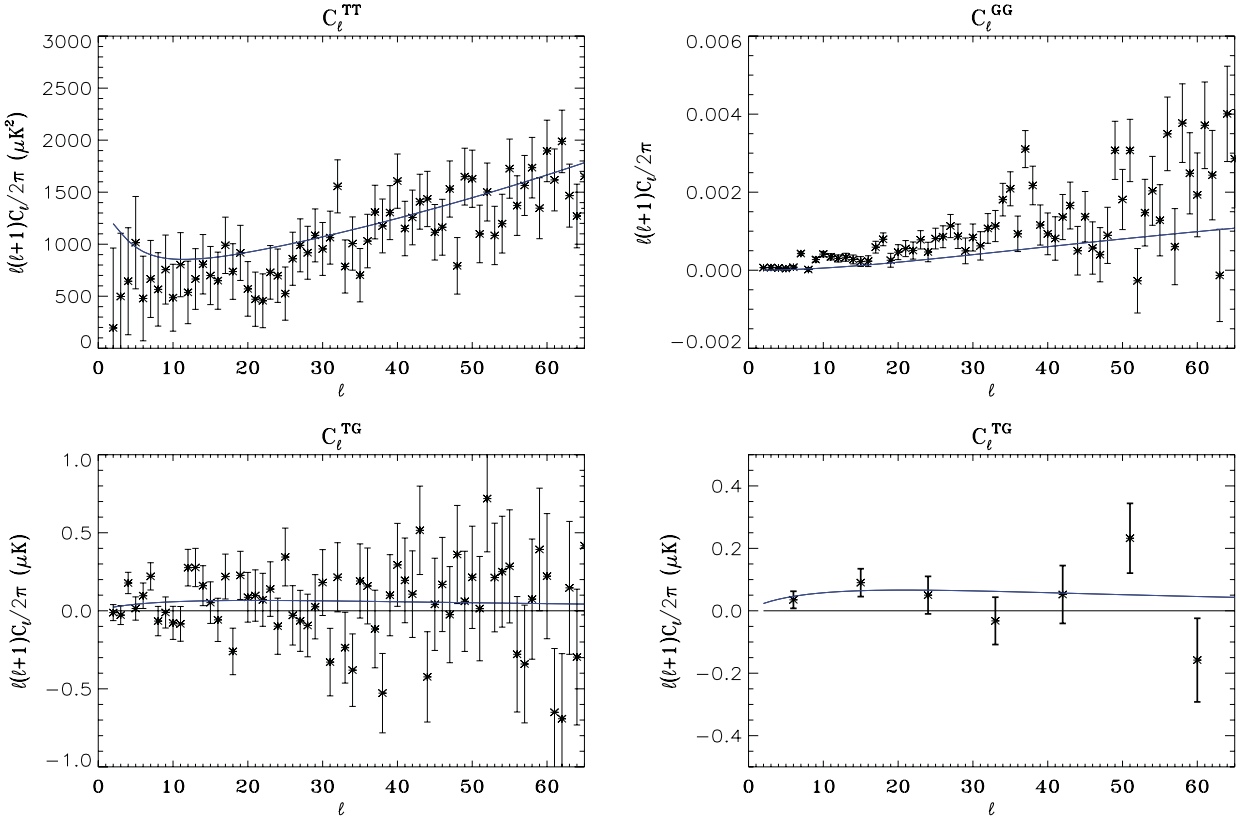

Figure 4. APS estimates from *WMAP* 7-yr and NVSS data for the 2.5 mJy flux cut. The upper panels show the auto-spectra, TT and GG, while the lower panels give the cross-spectra, TG, in the no binning case (left-hand panel) and in the binning case (right-hand panel). The blue solid lines are always the fiducial power spectra. The TG cross-spectrum in the lower-right panel is binned with $\Delta\ell = 9$ to make clearer the QML estimates with respect to the fiducial power spectrum (blue solid line) and the $C_\ell^{\rm TG} = 0$ (black solid line). We can note that the QML estimates for the GG auto-spectrum are slightly larger than the expected fiducial power spectrum.

non-negligible primordial non-Gaussianity, caused by the large-scale dependence of the non-Gaussian halo bias. Moreover, the value inferred for the coupling non-Gaussian parameter $f_{\rm NL}$ is much larger than the limits imposed by CMB analyses (e.g. Curto et al. 2011; Komatsu et al. 2011). The $f_{\rm NL}$ constraints derived from the CMB–LSS cross-correlation (Xia et al. 2010b) provide lower values, in better agreement with the CMB tests. In addition, these authors also showed that when other LSS data sets are used (in particular, the QSO sample of the SDSS; Richards et al. 2009), such non-Gaussian deviation is not found.

Our measurements of the TG spectrum are largely consistent with the previous investigation by Ho et al. (2008); however, there are some differences. For example, Ho et al. (2008) find a significant (2σ) excess in the lowest ℓ bin of the cross-correlation, while we see no evidence for such an excess.

5 DARK ENERGY CONSTRAINTS

In this section, we constrain the dark energy density Ω_Λ using the information contained in the ISW–LSS cross-correlation power spectrum, estimated through our QML. As in the most of previous literature (Pietrobon et al. 2006; Vielva et al. 2006), we approximate the errors on the measured $C_\ell^{\rm TG}$ as Gaussian and calculate the relative likelihoods of Ω_Λ using

$$-2\ln[\mathcal{L}(\Omega_\Lambda)] = \chi^2(\Omega_\Lambda) - \chi^2_{\rm min}, \tag{27}$$

where

$$\chi^2(\Omega_\Lambda) = \left[C_\ell^{\rm TG,obs} - C_\ell^{\rm TG}(\Omega_\Lambda)\right] \mathbf{C}^{-1}_{\ell\ell'} \left[C_{\ell'}^{\rm TG,obs} - C_{\ell'}^{\rm TG}(\Omega_\Lambda)\right]. \tag{28}$$

Here $C_\ell^{\rm TG,obs}$ are the unbinned estimates of the cross-correlation power spectrum and $C_\ell^{\rm TG}(\Omega_\Lambda)$ are the theoretical predicted power spectrum. The matrix $\mathbf{C}_{\ell\ell'}$ is the covariance matrix between different multipoles, which allows for correlations among non-diagonal terms which arise in the presence of masks. $\chi^2_{\rm min}$ is the minimum value of χ^2 with respect to Ω_Λ.

We compare the likelihoods obtained by different prescriptions for the covariance matrix. The first prescription is to use the *unbinned* QML estimates and the Fisher matrix as its covariance matrix:

$$\mathcal{C}^F_{\ell\ell'} = (\mathbf{F}^{-1})^{\rm TG\,TG}_{\ell\ell'}. \tag{29}$$

An alternative prescription is to construct the covariance matrix $\mathcal{C}$ by averaging over Monte Carlo realizations of the maps. For every model Ω_Λ, we can define the covariance $\mathcal{C}$ with N simulated CMB and LSS maps,

$$\mathcal{C}_{\ell\ell'}(\Omega_\Lambda) = \sum_{i=0}^{N} \frac{\left[C^{\rm TG}_{\ell,i}(\Omega_\Lambda) - \bar{C}^{\rm TG}_\ell(\Omega_\Lambda)\right]\left[C^{\rm TG}_{\ell',i}(\Omega_\Lambda) - \bar{C}^{\rm TG}_{\ell'}(\Omega_\Lambda)\right]}{N}, \tag{30}$$

where $C^{\rm TG}_{\ell,i}$ are the estimates for every single realization i and $\bar{C}^{\rm TG}_\ell$ is their average over the simulations which should correspond to their

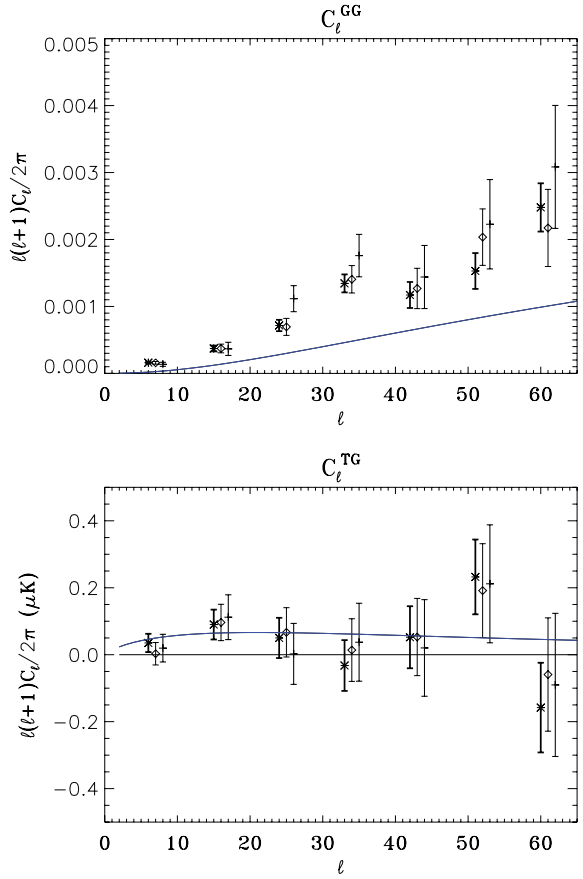

Figure 5. Comparison of the binned GG and TG spectra for three thresholds in flux, i.e. 2.5 mJy (stars with thick error bars), 5 mJy (diamonds with grey error bars) and 10 mJy (cross with error bars). The results appear largely consistent, while the errors increase as the number of sources decrease.

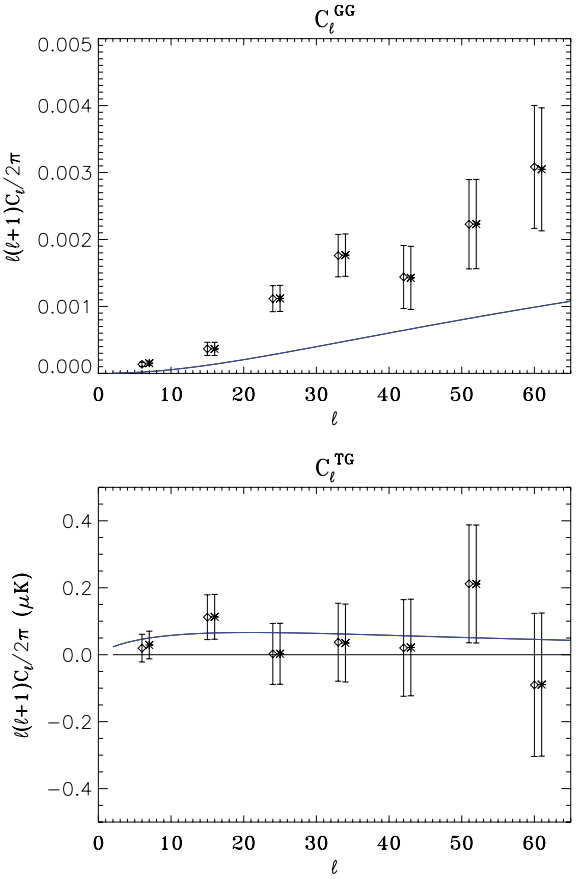

Figure 6. Comparison of the binned GG and TG spectra when the declination correction is included (diamonds) or not included (cross), assuming a flux cut of 10 mJy.

theoretical value. However, we expect the covariance matrix not to depend strongly on the cosmological model and therefore one can just consider the case with $\Omega_\Lambda = 0$, and since $\bar{C}_\ell^{TG}(\Omega_\Lambda = 0) = 0$, the covariance becomes

$$\mathcal{C}_{\ell\ell'}^{MC} = \sum_{i=0}^{N} \frac{C_{\ell,i}^{TG} C_{\ell',i}^{TG}}{N}. \quad (31)$$

We can build $\mathcal{C}_{\ell\ell'}$ in equation (31) either by using random realizations of only the CMB maps *and the single, true* NVSS map, or by creating realizations of both CMB and LSS maps. In both cases, we generate our covariances on 1000 realizations, as done by Vielva et al. (2006). We also examine how the probability contours for Ω_Λ depend on the various assumptions such as the threshold flux cut used for the NVSS map or the source redshift distribution.

We evaluate the likelihood with the various different prescriptions by sampling the χ^2 on values of Ω_Λ, $0 < \Omega_\Lambda < 0.95$. The other cosmological parameters are kept fixed to the values determined by *WMAP* (Larson et al. 2011) for the standard ΛCDM model. As a default NVSS description, the equation (24) model is assumed, with a bias of 1.98.

By adopting the Fisher matrix prescription in equation (29), as tightest constraint we obtain $\Omega_\Lambda = 0.78^{+0.13\,(0.16)}_{-0.18\,(0.47)}$ at $1(2)\sigma$ confidence level (CL) for the lowest flux threshold of 2.5 mJy, see the blue dashed line in Fig. 8. An Einstein–de Sitter universe is disfavoured at more than 2σ CL for the lowest flux threshold in NVSS, consistent with earlier measurements. Note that the conditional probabilities for Ω_Λ agree for the different flux thresholds considered.

By building the covariance through realizations of the CMB maps while keeping the NVSS map fixed, we obtain the probability distribution given by the red dotted line in Fig. 9. We find $\Omega_\Lambda = 0.72^{+0.18\,(0.22)}_{-0.23\,(0.55)}$ at $1(2)\sigma$ CL. Using instead the covariance derived from realizations of both CMB and LSS maps, we obtain the probability distribution given by the black solid line in Fig. 9 we find $\Omega_\Lambda = 0.82^{+0.10\,(0.13)}_{-0.16\,(0.39)}$ at $1(2)\sigma$ CL. Note that the constraint based on the Fisher covariance is tighter than the one based on a Monte Carlo covariance keeping fixed the NVSS map, but looser than the Monte Carlo covariance obtained with CMB and LSS uncorrelated maps. Overall, the three likelihood prescriptions are consistent, although some of the differences might be ascribed to the (unexplained) discrepancy between the C_ℓ^{GG} estimates and the theoretical predictions, on which the Monte Carlos are based.

Given the agreement among the three different likelihood prescriptions, we can use the Fisher prescription for the covariance to test other dependences of the analysis. In Fig. 10 we verify the importance of taking into account the shot noise in the NVSS map: by not taking into account the shot noise the probability contours for Ω_Λ would be much tighter, even for the maps with the most sources. We then study the impact of approximating the signal covariance matrix (and consequently the Fisher matrix) as block diagonal, i.e. considering $C_\ell^{TG} = 0$ for the fiducial underlying model. This approximation is not essential for our approach, whereas it is necessary for Padmanabhan et al. (2005) in which only C_ℓ^{TG} is estimated. As

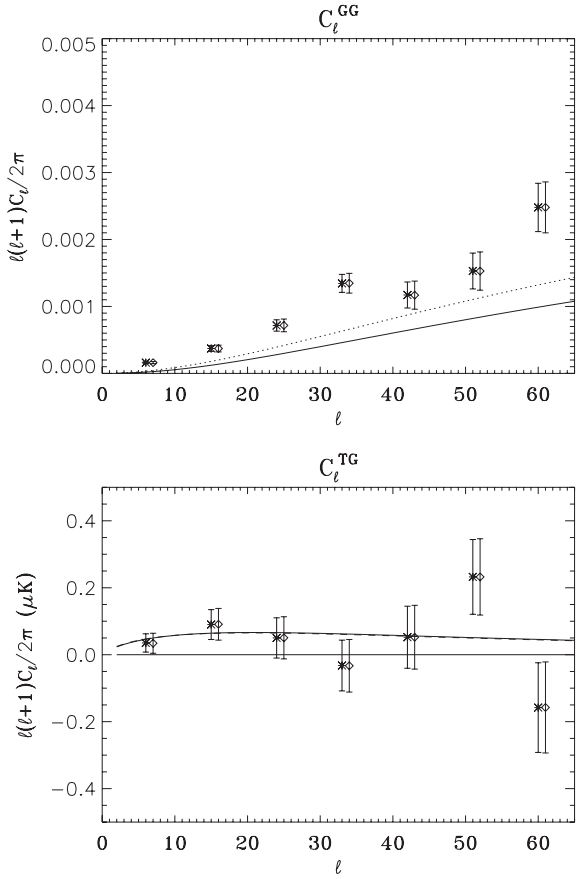

Figure 7. Comparison of the binned GG and TG spectra for the fiducial model (black solid line and stars) and the one with a redshift-dependent bias with the CENSORS source distribution (black dotted line and diamonds). Note how the estimates are stable with respect to the change in the fiducial model, and how an evolving bias could alleviate in part the tension between the theoretical GG predictions and the NVSS estimates.

mentioned in Section 2.3, the difference in the power spectrum estimates is barely visible and we have verified by Monte Carlo that this approximation does not alter the optimality of the method. On the real data considered here, Fig. 11 shows how the constraints with the full covariance and Fisher are a bit tighter than those with the block diagonal assumption. As already noted in Gruppuso et al. (2009), conditional probability slices are much more sensitive to small changes than QML estimates.

In Fig. 12 we compare the results obtained with the redshift distribution estimated with CENSORS data by de Zotti et al. (2010) in equation (25), including a redshift-dependent bias as from equation (26), with the one adopted by Ho et al. (2008), with an effective bias of 1.98.

6 DISCUSSIONS AND CONCLUSIONS

We have developed an optimal estimator for the APS of the cross-correlation between CMB and maps of LSS, which in parallel estimates their auto-spectra. This has been tested using an ensemble of randomly generated maps, and we have demonstrated the robustness of the QML estimates for the TT, TG and GG power spectra. Our QML implementation extend similar optimal estimators limited only to the galaxy auto-power spectrum (Blake et al. 2004) or only to the cross-correlation power spectrum (Padmanabhan et al. 2005).

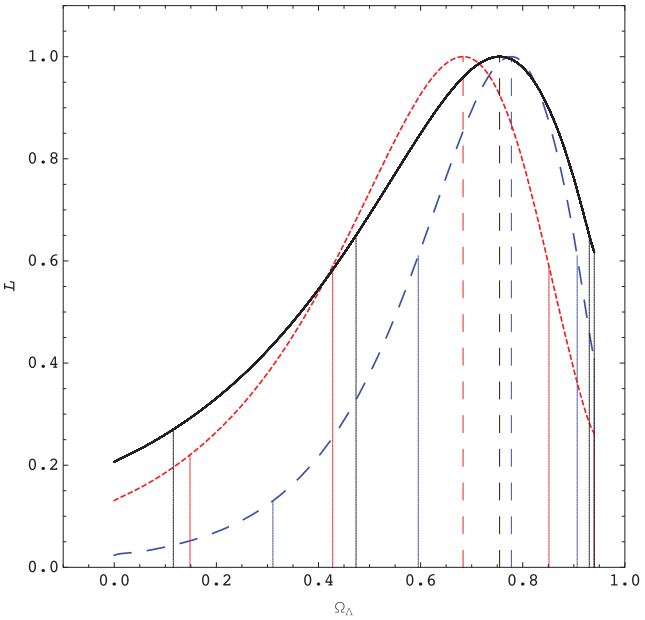

Figure 8. The likelihood for Ω_Λ obtained by the Fisher prescription in equation (29), with the 95 and 68 per cent CL for the threshold flux of 2.5 mJy (blue dashed line), 5 mJy (red dotted line) and 10 mJy (black solid line) in NVSS, respectively.

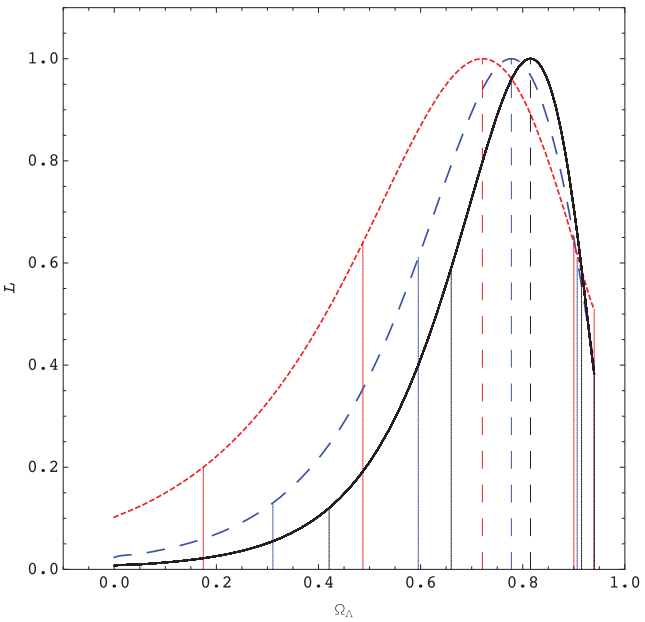

Figure 9. Comparison of likelihood contours for Ω_Λ obtained by the Fisher prescription (blue dashed line), the covariance computed by the Monte Carlo for CMB only (red dotted line) and for both CMB and LSS (black solid line). The threshold flux in NVSS has been chosen to be 2.5 mJy.

We have applied our method to *WMAP* 7-yr and NVSS data, the best public data sets at present for studying the ISW cross-correlations. Our QML implementation, described in Section 2, allows us to measure the cross-correlation power spectrum optimally and to exploit the full cosmological information contained in the maps, though our analysis is limited to a pixel resolution of 1°.8. While the NVSS map contains known declination systematics, we correct for these and find, as has earlier work, that they appear to have little effect on the measured cross-correlations. In agreement

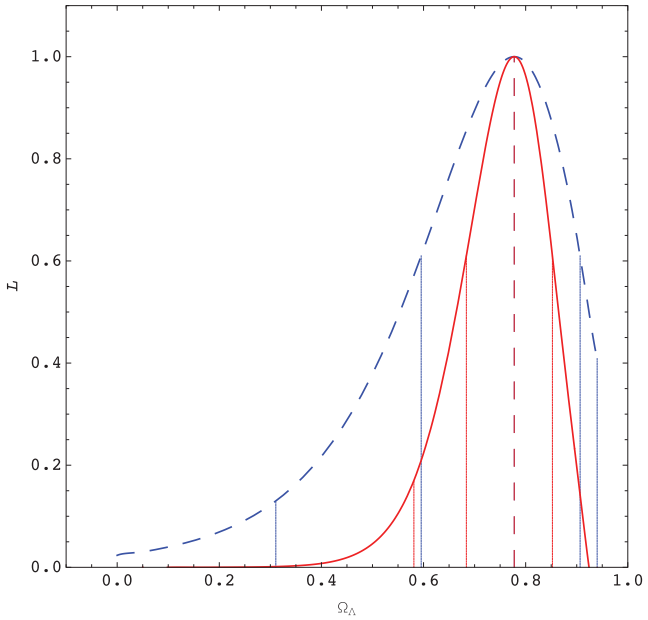

Figure 10. Comparison of likelihood contours for Ω_Λ obtained by the Fisher prescription in equation (29) when accounting (dashed line) and when not accounting (solid line) for shot noise in NVSS data. The threshold flux in NVSS has been chosen as 2.5 mJy.

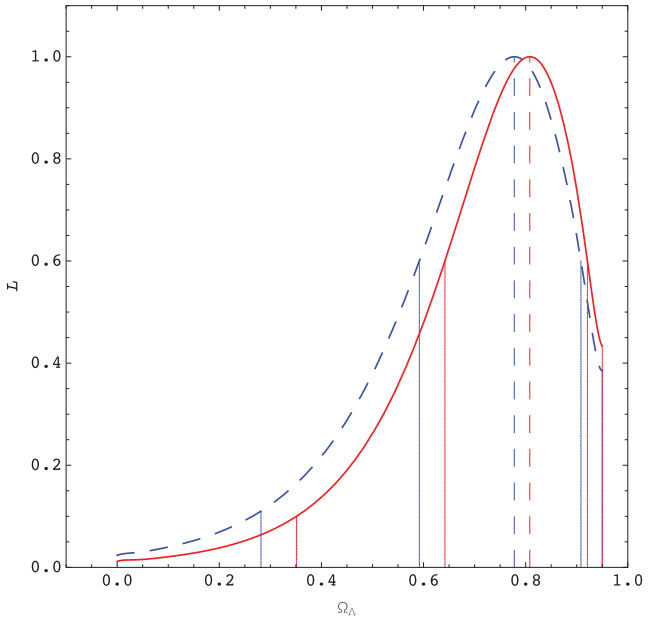

Figure 11. Comparison of likelihood contours for Ω_Λ obtained by the Fisher prescription in equation (29) when considering the full covariance (red solid line) and when using the approximation of a block diagonal signal covariance. The threshold flux in NVSS has been chosen as 2.5 mJy.

with previous studies, we detect a non-zero cross-correlation, and have also seen a certain excess in the NVSS auto-APS compared to that expected theoretically.

We have translated these measurements into the quantitative constraints on the fraction of dark energy in a ΛCDM model which can be obtained only by the cross-correlation of *WMAP* and NVSS, estimating Ω_Λ while keeping fixed all the other cosmological parameters to the *WMAP* 7-yr best-fitting values (Larson et al. 2011). We have compared three different prescriptions for estimating the

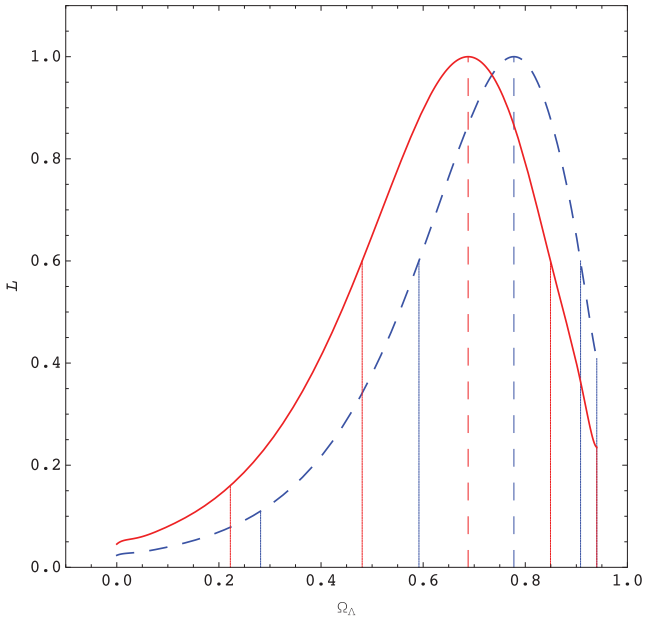

Figure 12. Comparison of likelihood contours for Ω_Λ obtained by the Fisher prescription in equation (29) for the two choices of redshift distributions: dashed for equation (24) and solid for equation (25). The threshold flux in NVSS has been chosen as 2.5 mJy.

covariances: using the Fisher matrix computed by our QML, on Monte Carlo realizations of the CMB maps only and creating Monte Carlo realizations of both CMB and LSS maps. We have found good agreement among the Ω_Λ probability contours obtained from these three different likelihood prescriptions. The width of this probability contour depends mainly on the flux threshold and associated level of Poisson noise in the NVSS map, but the signal amplitude seems largely independent of the flux. The constraint from the likelihood prescription based on the Fisher matrix we derive from the cross-correlation between *WMAP* 7-yr and NVSS data is $\Omega_\Lambda = 0.78^{+0.13\,(0.16)}_{-0.18\,(0.47)}$ at $1(2)\sigma$ CL for the lowest flux threshold of 2.5 mJy. Such a value is quite consistent with the concordance cosmology. This result agrees with that expected from a typical survey with sky fraction and noise properties as the NVSS, and agrees with Vielva et al. (2006), but is somewhat weaker than the one obtained by the non-optimal analysis by Pietrobon et al. (2006) based on needlets. It is not clear if this discrepancy is due to the lower resolution considered here or the neglect of shot noise in the NVSS map in the analysis by Pietrobon et al. (2006).

ACKNOWLEDGMENTS

We wish to thank G. de Zotti for useful discussions on NVSS and S. Matarrese for stimulating discussions on the bias. FS, FF and AG wish to thank Adriano De Rosa for useful suggestions on the QML implementation. We acknowledge the use of the SP6 supercomputer at CINECA under the agreement INAF/CINECA and LFI/CINECA, and the use of the HEALPIX software and analysis package (Gorski et al. 2005). We thank the other Planck/LFI developers of the BOLPOL code from which the BOLISW code has inherited some routines whose use is therefore acknowledged. We also acknowledge the use of the Legacy Archive for Microwave Background Data Analysis (LAMBDA); support for LAMBDA is provided by the NASA Office of Space Science. This work is supported by ASI through ASI/INAF Agreement I/072/09/0 for

the Planck LFI Activity of Phase E2. PV, RBB, AMC and EMG acknowledge partial financial support from the Spanish Ministerio de Ciencia e Innovación project AYA2010-21766-C03-01 and the Consolider Ingenio-2010 Programme project CDS2010-00064, and PV also acknowledges financial support from the Ramón y Cajal programme. RGC is supported by STFC grant ST/H002774/1.

REFERENCES

Afshordi N., Loh Y. S., Strauss M. A., 2004, Phys. Rev. D, 69, 083524
Barreiro R. B., Vielva P., Hernández-Monteagudo C., Martínez-González E., 2008, IEEE J. Sel. Top. Signal Process., 2, 747
Blake C., Wall J., 2002, MNRAS, 329, 37
Blake C., Ferreira P. G., Borrill J., 2004, MNRAS, 351, 923
Boughn S. P., Crittenden R. G., 2002, Phys. Rev. Lett., 88, 021302
Boughn S. P., Crittenden R. G., 2004, Nat, 427, 45
Boughn S. P., Crittenden R. G., Turok N. G., 1998, New Astron., 3, 275
Boughn S. P., Crittenden R. G., Koehrsen G. P., 2002, ApJ, 580, 672
Brookes M. H., Best P. N., Peacock J. A., Rottgering H. J. A., Dunlop J. S., 2008, MNRAS, 385, 1297
Condon J. J., Cotton W. D., Greisen E. W., Yin Q. F., Perley R. A., Taylor G. B., Broderick J. J., 1998, AJ, 115, 1693
Crittenden R. G., Turok N., 1996, Phys. Rev. Lett., 76, 575
Curto A., Martínez-González E., Barreiro R. B., Hobson M. P., 2011, MNRAS, 417, 488
de Zotti G., Massardi M., Negrello M., Wall J., 2010, A&AR, 18, 1
Dunkley J. et al. (WMAP), 2009, ApJS, 180, 306
Dunlop J. S., Peacock J. A., 1990, MNRAS, 247, 19
Dupé F. X., Rassat A., Starck J. L., Fadili M. J., 2011, A&A, 534, 151
Eisenstein D. J. et al., 2005, ApJ, 633, 550
Fosalba P., Gaztañaga E., Castander F. J., 2003, ApJ, 597, 89
Francis C. L., Peacock J. A., 2010, MNRAS, 406, 2
Giannantonio T., Scranton R., Crittenden R. G., Nichol R. C., Boughn S. P., Myers A. D., Richards G. T., 2008, Phys. Rev. D, 77, 123520
Gold B. et al., 2011, ApJS, 192, 15
Gorski K. M., Hivon E., Banday A. J., Wandelt B. D., Hansen F. K., Reinecke M., Bartelmann M., 2005, ApJ, 622, 759
Gruppuso A., De Rosa A., Cabella P., Paci F., Finelli F., Natoli P., De Gasperis G., Mandolesi N., 2009, MNRAS, 400, 1
Gruppuso A., Finelli F., Natoli P., Paci F., Cabella P., De Rosa A., Mandolesi N., 2011, MNRAS, 411, 3
Hernández-Monteagudo C., 2010, A&A, 520, 101
Ho S., Hirata C., Padmanabhan N., Salijak U., Bahcall N. A., 2008, Phys. Rev. D, 78, 043519
Jarosik N. et al., 2011, ApJS, 192, 14
Kofman L. A., Starobinsky A. A., 1985, Soviet Astron. Lett., 11, 271
Komatsu E. et al., 2011, ApJS, 192, 18
Larson D. et al., 2011, ApJS, 192, 16
Laureijs R. et al., 2009, preprint (arXiv:0912.0914)
Matarrese S., Coles P., Lucchin F., Moscardini L., 1997, MNRAS, 286, 115
McEwan J. D., Vielva P., Hobson M. P., Martínez-González E., Lasenby A. N., 2007, MNRAS, 376, 1211
McEwan J. D., Wiaux Y., Hobson M. P., Vandergheynst P., Lasenby A. N., 2008, MNRAS, 384, 1289
Moscardini L., Coles P., Lucchin F., Matarrese S., 1998, MNRAS, 299, 55
Nolta M. R. et al. (WMAP Collaboration), 2004, ApJ, 608, 10
Paci F., Gruppuso A., Finelli F., Cabella P., De Rosa A., Mandolesi N., Natoli P., 2010, MNRAS, 407, 399
Padmanabhan N., Hirata C. M., Seljak U., Schlegel D., Brinkmann J., Schneider D. P., 2005, Phys. Rev. D, 72, 043525
Perlmutter S. et al., 1999, ApJ, 517, 565
Pietrobon D., Balbi A., Marinucci D., 2006, Phys. Rev. D, 74, 043524
Planck Collaboration, 2006, preprint (arXiv:0604.069)
Richards G. T. et al., 2009, ApJS, 180, 67
Riess A. et al., 1998, AJ, 116, 1009
Sachs R. K., Wolfe A. M., 1967, ApJ, 147, 73
Sawangwit U., Shanks T., Cannon R. D., Croom S. M., Ross N. P., Wake D. A., 2010, MNRAS, 402, 2228
Tegmark M., 1997, Phys. Rev. D, 55, 5895
Tegmark M., de Oliveira-Costa A., 2001, Phys. Rev. D, 64, 063001
Tegmark M. et al., 2004, Phys. Rev. D, 69, 103501
Vielva P., Martínez-González E., Tucci M., 2006, MNRAS, 365, 891
Xia J.-Q., Viel M., Baccigalupi C., De Zotti G., Matarrese S., Verde L., 2010a, ApJ, 717, L17
Xia J.-Q., Bonaldi A., Baccigalupi C., De Zotti G., Matarrese S., Verde L., Viel M., 2010b, J. Cosmol. Astropart. Phys., 8, 13

This paper has been typeset from a TEX/LATEX file prepared by the author.